INTERNATIONAL JOURNAL FOR NUMERICAL METHODS IN FLUIDS
Int. J. Numer. Meth. Fluids **30**: 653–674 (1999)

A 2D BOUNDARY ELEMENT METHOD FOR SIMULATING THE DEFORMATION OF AXISYMMETRIC COMPOUND NON-NEWTONIAN DROPS

E.M. TOOSE[a,*], B.J. GEURTS[b] AND J.G.M. KUERTEN[b]

[a] *Rheology Group, Department of Applied Physics, J.M. Burgers Centre, University of Twente, PO Box 217, 7500 AE Enschede, Netherlands*
[b] *Department of Applied Mathematics, J.M. Burgers Centre, University of Twente, PO Box 217, 7500 AE Enschede, Netherlands*

SUMMARY

The boundary integral formulation of the solution to the Stokes equations is used to describe the deformation of small compound non-Newtonian axisymmetric drops suspended in a Newtonian fluid that is subjected to an axisymmetric flow field. The non-Newtonian stress is treated as a source term in the Stokes equations, which yields an extra integral over the domains containing non-Newtonian material. By transforming the integral representation for the velocity to cylindrical co-ordinates and performing the integration over the azimuthal direction analytically, the dimension of the problem can be reduced from three to two. A boundary element method for the remaining two-dimensional problem aimed at the simulation of the deformation of such axisymmetric compound non-Newtonian drops is developed. Apart from a numerical validation of the method, simulation results for a drop consisting of an Oldroyd-B fluid and a viscoelastic material are presented. Moreover, the method is extended to compound drops that are composed of a viscous inner core encapsulated by a viscoelastic material. The simulation results for these drops are verified against theoretical results from literature. Moreover, it is shown that the method can be used to identify the dominant break-up mechanism of compound drops in relation to the specific non-Newtonian character of the membrane. Copyright © 1999 John Wiley & Sons, Ltd.

KEY WORDS: non-Newtonian; drops; boundary element method; Stokes flow

1. INTRODUCTION

Deformable particles, such as gas bubbles, liquid drops and biological cells, appear in a wide range of technological and medical applications. Examples include advanced material processing, food processing and pharmaceutical manufacturing. As the deformability of these particles strongly determines the macroscopic properties of the material it composes, much research emphasis has been put on the description of the deformation process of deformable drops (see e.g. Rallison [1] and Stone [2] for a survey). If the drops are sufficiently small, the dynamics of these drops can be analyzed through an investigation of the Stokes equations since the corresponding Reynolds number is small enough to justify neglecting inertia forces. Most theoretical work has been directed towards the case that the drop and its surrounding fluid

---

* Correspondence to: Faculty of Applied Mathematics, University of Twente, PO Box 217, 7500 AE Enschede, Netherlands.

CCC 0271–2091/99/140653–22$17.50

Received February 1997
Revised May 1997

consist of different Newtonian fluids in which the interface between the drop and the surrounding fluid is considered infinitely thin and characterized by a constant surface tension. The velocity field can, in these cases, be expressed in terms of a boundary integral over the surface of the drop [3,4]. In this paper, this boundary integral approach is extended for axisymmetric flow in two ways. First, non-Newtonian fluids are incorporated in the description, which gives rise to additional volume integrals. Secondly, compound drops are allowed for, which are composed of multiple layers of (non-)Newtonian material. In this way, the method can be used for non-Newtonian drops as well as for e.g. red blood cells or vesicles in which the membrane is modelled as an interface of finite thickness with certain non-Newtonian properties (Brunn [5] and Smeulders [6]). It will be shown that the specific non-Newtonian character of the layers has a significant effect on the dynamics and break-up mechanism of the drop.

The deformation of neutrally buoyant viscous drops with interfacial tension in viscous extensional flows at low Reynolds number was first studied analytically by Taylor [7]. In his analytical work he starts with the solution to the Stokes equation in terms of an expansion in spherical harmonics (Lamb [8]). By approximating the shape of the drop in terms of spherical harmonics one may find a first-order approximation of the deformation of the drop and the viscosity of dilute suspension of drops. This technique was refined (Cox [9] and Barthès-Biesel [10]) and extended to other situations, such as viscous drops surrounded by a viscoelastic shell (Brunn [5]) or double concentric viscous drops (Stone and Leal [11]). An extensive study of the effects of the interface properties of viscous drops on the rheology of a dilute emulsion was performed by Oldroyd [12,13]. For this purpose, a so-called cell model was introduced, which enables the study of this problem in the frequency domain. The linear character of the flow problem in the frequency domain allowed Palierne [14] to extend the work of Oldroyd to linear viscoelastic drops with interfacial tension. A different approach was taken by Roscoe [15] who used the work of Jeffery [16] on solid ellipsoidal particles in a viscous flow to describe the deformation of viscoelastic particles.

Apart from theoretical studies, the deformation of Newtonian drops in viscous extensional flows at low Reynolds number was first studied numerically by Youngren [17] using a boundary element method. For drops composed of Newtonian fluids alone, this method involves only quantities at the boundaries and hence the dimension of the computational problem is reduced by one in these applications. The method has extensively been used by others as well in order to simulate the behaviour of Newtonian drops in simple flow fields. Apart from improvements in the numerical method (Huang [18]), recent studies have tackled more complicated flow problems (e.g. break-up of drops, Tjahjadi [19]) and incorporated additional physical phenomena (e.g. the effects due to surfactants, Stone [20] and the elasticity of the membrane, Li [27]). Recently, the boundary element method was also used to simulate concentrated emulsions of viscous drops in shear flow (Xiofan Li *et al.* [21] and Loewenberg and Hinch [22]) and double concentric viscous drops (Stone and Leal [11]).

In many applications, however, the drop consists of a non-Newtonian fluid. Examples include polymer blends, suspensions of vesicles and biological fluids such as blood. The development of the boundary integral method in these cases is much more complicated due to the domain integral that arises from the non-Newtonian contributions. This implies the introduction of a grid covering the layers of the drop containing non-Newtonian fluids, next to the definition of discrete points on the interface, and adds considerably to the numerical cost of simulations of compound non-Newtonian drops. However, compared with a more direct (finite difference) discretization of the Stokes equations, which would also require a grid covering the much larger Newtonian region exterior to the drop, the boundary integral method for non-Newtonian drops has a number of important advantages. The incompressibility of the fluids is fully incorporated into the expression for the velocity field and does not require some sort of 'pressure-correction' as occurs in many direct numerical methods for simulating unsteady incompressible flows. The boundary integral method is also more flexible and accurate with respect to modelling the boundary geometries and boundary conditions. In particular, the conditions on the solution at infinity are explicitly taken care of in the boundary integral method, whereas a suitable but approximate condition at a finite distance needs to be introduced in combination with a finite difference method. In addition, the boundary integral method is especially suited for simulating time-dependent problems with moving boundaries. Moreover, in several applications the region containing a non-Newtonian fluid forms only a small portion of the flow problem, e.g. a vesicle in which the drop is formed by a Newtonian fluid that is encapsulated by a non-Newtonian lipid bilayer [6], and the boundary integral method can be used effectively. Bush [23,24] adopted the boundary element method to analyze extrusion experiments with non-Newtonian fluids. The extension of the method to non-Newtonian drops is valid provided certain assumptions on the smoothness of the non-Newtonian stress tensor are satisfied. These were numerically verified for a two-dimensional drop [25] and for a three-dimensional axisymmetric drop [26]. In the current paper, the extension to compound non-Newtonian drops immersed in a Newtonian fluid in axisymmetric flow is considered. The method is illustrated by comparing simulation results for non-Newtonian drops with theoretical results from literature.

The organization of this paper is as follows. In Section 2, the governing equations are presented and the velocity field is expressed in terms of a domain integral involving the non-Newtonian stress tensor and a boundary integral arising from the Newtonian contributions. Section 3 is devoted to the numerical method used to simulate the deformation of a compound drop. Simulation results for both Newtonian and non-Newtonian compound drops are presented in Section 4. Finally, the findings are summarized in Section 5.

2. GOVERNING EQUATIONS

This section presents the basic equations governing Stokes flow of compound non-Newtonian drops and arrives at the fundamental expression for the velocity field corresponding to axisymmetric deformation processes.

An isotropic axisymmetric compound non-Newtonian drop placed in an unbounded Newtonian fluid with viscosity η, which is subjected to a linear elongational flow is considered. The axis of symmetry of the drop is assumed to coincide with the axis of symmetry of the external flow field, which is defined by:

$$u_1^\infty = Gx_1, \qquad u_2^\infty = -\frac{1}{2}Gx_2, \qquad u_3^\infty = -\frac{1}{2}Gx_3, \tag{2.1}$$

with u_j^∞ the jth component of the velocity field with respect to a Cartesian co-ordinate frame $\{e_1, e_2, e_3\}$ and G is the magnitude of the flow. The compound drop consists of K concentric layers, each containing some (non-)Newtonian material. The volumes occupied by the unbounded Newtonian fluid outside the drop and the different layers, counted from the outside to the inside, are denoted by $V^{(0)}$ and $V^{(1)}, V^{(2)}, \ldots, V^{(K)}$ respectively (see Figure 1). Along the interface $S^{(l)}$ between the domains $V^{(l-1)}$ and $V^{(l)}$, $l = 1, \ldots, K$, there acts a constant interfacial tension $\sigma^{(l)}$. The interface $S^{(l)}$ corresponds to the outer drop interface. The fluid is incompressible and buoyancy is considered to be absent, i.e. it is assumed that the densities of all fluids composing the drop are equal. The initial configuration of the drop is taken to be a set of concentric spheres with radii $R^{(l)}$, $l=1,\ldots,K$. Throughout the work, dimensionless variables will be used: all lengths are scaled with the initial outer drop radius $R^{(1)}=a$, velocities by aG and viscosities by η (Li *et al.* [27]). In changing to dimensionless variables it is convenient to introduce the following dimensionless parameters:

$$C^{(l)}=\frac{\eta Ga}{\sigma^{(l)}}, \qquad \lambda^{(l)}=\frac{\eta^{(l)}}{\eta} \quad \text{and} \quad \kappa^{(l)}=\frac{R^{(l)}-R^{(l+1)}}{a}; \quad l=1,\ldots,K, \tag{2.2}$$

where $C^{(l)}$ is the capillary number of the lth interface, which is a measure of the ratio between the viscous and interfacial tension stresses. The parameter $\lambda^{(l)}$ is the ratio between the viscosity, $\eta^{(l)}$ in the lth domain and the exterior viscosity η and $\kappa^{(l)}$ are the ratio of the thickness of the undeformed spherical layer $V^{(l)}$ and the outer radius of the drop, where for convenience $R^{(K+1)}=0$ is introduced. In order to characterize the degree of distortion of the interfaces due to the external velocity field, one commonly defines a deformation parameter $D^{(l)}$ as:

$$D^{(l)}=\frac{r^{(l)}_{\max}-r^{(l)}_{\min}}{r^{(l)}_{\max}+r^{(l)}_{\min}}; \quad l=1,\ldots,K, \tag{2.3}$$

where $r^{(l)}_{\max}$ and $r^{(l)}_{\min}$ denote the longest and shortest principal axes of the lth deformed interface.

The flow in and around a compound non-Newtonian drop as introduced above is governed by the Stokes equations if the Reynolds number $Re=(\rho a^2G)/\eta$ (with ρ being the density) is sufficiently small (Pozrikidis [28]). In particular, the basic equations read:

$$\partial_j u_j=0; \qquad \partial_j \pi_{ij}=0, \tag{2.4}$$

with π_{ij} the total stress tensor and $\partial_j=\partial/\partial x_j$. In Equation (2.4), as in the rest of this paper, the summation convention is adopted that implies summation over repeated indices. The Stokes equations given above are further supplemented with suitable matching conditions at the interfaces $S^{(l)}$ and asymptotic conditions as $|\boldsymbol{x}|\to\infty$. As the different layers of the drop can consist of different types of non-Newtonian materials, it is convenient to distinguish between a set of local stress tensors $\pi^{(l)}_{ij}$, $l=1,\ldots,K$, corresponding to the total stress tensor in the domain $V^{(l)}$, i.e. $\pi^{(l)}_{ij}=\pi_{ij}$ if $\boldsymbol{x}\in V^{(l)}$. The superscript ($l$) will be used for the other flow quantities as well to indicate the domain of definition.

In the domain $V^{(l)}$ the total stress tensor π_{ij} is decomposed as:

$$\pi^{(l)}_{ij}=-\delta_{ij}P^{(l)}+\lambda^{(l)}\dot{\gamma}^{(l)}_{ij}+\tilde{\tau}^{(l)}_{ij}, \quad i=1,\ldots,3, \tag{2.5}$$

where $P^{(l)}$ is the isotropic pressure field and $\dot{\gamma}^{(l)}_{ij}$ the rate of strain tensor:

$$\dot{\gamma}^{(l)}_{ij}=\partial_i u^{(l)}_j+\partial_j u^{(l)}_i.$$

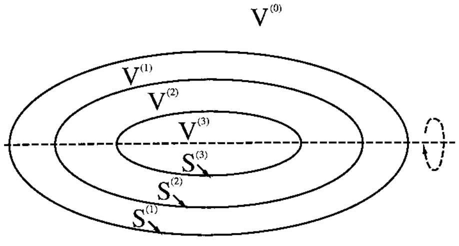

Figure 1. Schematic illustration of the different domains and interfaces.

The non-Newtonian part of the stress tensor $\tilde{\tau}_{ij}^{(l)}$ in (2.5) obeys a certain constitutive equation that describes the non-Newtonian character of the fluid motion. In this paper, focus is on the Maxwell model and a specific elastic model, although the method presented here can be extended to quite general rheological models. The Maxwell model finds its origin in polymer rheology and contains two parameters: a relaxation time $t_p^{(l)}$ and the polymer contribution to the zero shear rate viscosity $\eta_p^{(l)}$ [29]. The constitutive equation for this model is given by:

$$\mu_p^{(l)}\mathscr{D}_t\tilde{\tau}_{ij}^{(l)}+\tilde{\tau}_{ij}^{(l)}=\lambda_p^{(l)}\dot{\gamma}_{ij}^{(j)}, \tag{2.6}$$

where $\mathscr{D}_t$ denotes the upper convected time derivative (Bird [29]), $\mu_p^{(l)}=Gt_p^{(l)}$ the dimensionless relaxation time and $\lambda_p^{(l)}=\eta_p^{(l)}/\eta$. The total stress tensor $\pi_{ij}^{(l)}$ for this model corresponds to the well-known Oldroyd-B model (Bird [29]). The constitutive equation for the elastic model considered here is given by:

$$\tilde{\tau}_{ij}^{(l)}=c_1^{(l)}B_{ij}+c_2^{(l)}B_{ij}^{-1}, \tag{2.7}$$

where $c_1^{(l)}$ and $c_2^{(l)}$ are arbitrary constants. In expression (2.7), B_{ij} is the so-called left Cauchy–Green strain tensor, which is defined as:

$$B_{ij}=\frac{\partial \boldsymbol{x}_i}{\partial \boldsymbol{X}_l}\frac{\partial \boldsymbol{x}_l}{\partial \boldsymbol{X}_j}, \tag{2.8}$$

where $\boldsymbol{x}$ describes the present and $\boldsymbol{X}$ the initial configuration of the material. The total stress tensor $\pi_{ij}^{(l)}$ for this model is called the viscoelastic model for which the authors focus on two special cases. In the first case, identified as viscoelastic I, they set $c_2^{(l)}=0$, whereas in the second case $c_1^{(l)}=0$, which is referred to as viscoelastic II. In the literature, the first model is also called an ideal rubber model, in which $c_1^{(l)}$ is proportional to the number of cross-links in the rubber material (Bird [29]).

The identification of the non-Newtonian stress contribution to $\pi_{ij}^{(l)}$ is not unique. This can be used to simplify the subsequent formulation by incorporating a part of the Newtonian stress into the non-Newtonian stress. In particular, by redefining the non-Newtonian stress as:

$$\tilde{\tau}_{ij}^{(l)}\to\tilde{\tau}_{ij}^{(l)}+(\lambda^{(l)}-1)\dot{\gamma}_{ij}^{(l)},$$

$\lambda^{(l)}=1$ can be used in (2.5) without loss of generality (Toose *et al.* [25,26]). In the remainder of the paper, the redefined non-Newtonian stress tensor will be referred to as the extra stress tensor. Assuming that the Reynolds number is small, the fluid motion in the lth domain is governed by the inhomogeneous Stokes equations:

$$\begin{cases}\partial_{jj}u_i^{(l)}-\partial_i P^{(l)}=-\partial_j\tilde{\tau}_{ij}^{(l)}\\ \partial_j u_j^{(l)}=0.\end{cases} \tag{2.9}$$

The velocity and the total stress tensor satisfy the following matching and asymptotic conditions:

$$\begin{cases}[u_i]_{S^{(l)}}=0, \qquad C^{(l)}[\pi_{ij}n_j]_{S^{(l)}}=n_i^{(l)}\partial_j n_j^{(l)}, \quad \text{for } l=1,2,\ldots,K,\\ u_i\to u_i^{\infty}, \quad \text{as } |\boldsymbol{x}|\to\infty,\end{cases} \tag{2.10}$$

where $\boldsymbol{n}^{(l)}$ is the outward unit normal on $S^{(l)}$, $\partial_j n_j^{(l)}$ is the boundary curvature and $[\,\cdot\,]_{S^{(l)}}$ denotes the jump of the quantity between the brackets over the interface $S^{(l)}$ counted in the direction $\boldsymbol{n}^{(l)}$:

$$[f]_{S^{(l)}}=f^{(l)}(\boldsymbol{x})-f^{(l-1)}(\boldsymbol{x}), \quad (\boldsymbol{x})\to S^{(l)}. \tag{2.11}$$

As the time dependence does not appear explicitly in (2.9), a kinematic constraint is used that describes the fluid motion in the different domains. The motion of the domain $V^{(l)}$ (and its boundaries) is modelled by considering the domain as a set of material points. The trajectories of these points can be followed using a Lagrangian representation of the velocity:

$$d_t x_i = x_i^{(l)}(\boldsymbol{x}), \quad \forall \boldsymbol{x} \in V^{(l)}(t), \tag{2.12}$$

with d_t the material time derivative. For the evolution, Equations (2.6) and (2.12) initial conditions need to be specified. For the interfaces $S^{(l)}$, the authors start with a spherical shape, whereas for the non-Newtonian contribution to the stress tensor, they assume an isotropic stress distribution:

$$\tilde{\tau}_{ij}(0) = Q\delta_{ij}, \tag{2.13}$$

with Q being constant.

Assuming that the non-Newtonian stress tensor is known at time t, and interpreting the right-hand-side of (2.9) as a source term, a solution for the velocity at time t can be constructed in terms of boundary integral equations (Lorentz [3]). Following Ladyzhenskaya [4], it can be shown that the integral representation for the velocity is given by (Toose *et al.* [26]):

$$u_k(\boldsymbol{x}) = u_k^{\infty}(\boldsymbol{x}) + \sum_{l=1}^{K} \int_{V^{(l)}} J_{ik}(\boldsymbol{r}) \partial_j \tilde{\tau}_{ij}^{(l)}(\boldsymbol{y}) \, \mathrm{d}\boldsymbol{y} + \sum_{l=1}^{K} \int_{S^{(l)}} J_{ik}(\boldsymbol{r}) q_i^{(l)}(\boldsymbol{y}) \, \mathrm{d}S_y, \tag{2.14}$$

with $\boldsymbol{r} = \boldsymbol{x} - \boldsymbol{y}$, $J_{ik}(\boldsymbol{r})$ being Green's function for the Stokes problem [3] and $q_i^{(l)}$ a surface force that is defined as:

$$q_i^{(l)} = [\tilde{\tau}_{ij}]_{S^{(l)}} n_j^{(l)} - \frac{1}{C^{(l)}} n_i^{(l)} \partial_j n_j^{(l)}.$$

From the latter definition it can be seen that the interfacial tension and the discontinuity of the extra stress tensor across the surface $S^{(l)}$ lead to the surface force $q_i^{(l)}$.

The flow problem defined above remains axisymmetric in time, and hence one can reduce the dimension of the computational problem by transforming the integral equation (2.14) to cylindrical co-ordinates (Toose *et al.* [26]). To perform this transformation it is convenient to define cylindrical co-ordinates:

$$\begin{cases} x_1 = \bar{x}_1, \\ x_2 = \bar{x}_2 \cos(\bar{x}_3), \\ x_3 = \bar{x}_2 \sin(\bar{x}_3), \end{cases} \tag{2.15}$$

where $\bar{x}_1$, $\bar{x}_2$ and $\bar{x}_3$ indicate the axial, radial and azimuthal components respectively. Observe that $(\bar{x}_1, \bar{x}_2, \bar{x}_3)$ are used instead of the more common (x, r, ϕ) in view of the summation convention. In the sequel, corresponding components with respect to cylindrical co-ordinates are denoted with an overbar.

By transforming the integral expression (2.14) to cylindrical co-ordinates and performing the integration over the azimuthal direction analytically, the following integral equation is obtained [26]:

$$\bar{u}_\alpha(\bar{\boldsymbol{x}}) = \bar{u}_\alpha^{\infty}(\bar{\boldsymbol{x}}) + \sum_{l=1}^{K} \int_{\bar{V}^{(l)}} M_\alpha^\beta(\bar{\boldsymbol{r}}) \bar{\partial}_\gamma \bar{\tilde{\tau}}_{\beta\gamma}^{(l)}(\bar{\boldsymbol{y}}) \bar{y}_2 \, \mathrm{d}\bar{y}_2 \, \mathrm{d}\bar{y}_1 + \sum_{l=1}^{K} \int_{\bar{S}^{(l)}} M_\alpha^\beta(\bar{\boldsymbol{r}}) \bar{q}_\beta^{(l)}(\bar{\boldsymbol{y}}) \bar{y}_2 \, \mathrm{d}\ell_y, \tag{2.16}$$

where $\bar{V}^{(l)}$ and $\bar{S}^{(l)}$ are the integration domains in cylindrical co-ordinates, which correspond to $V^{(l)}$ and $S^{(l)}$ respectively. In the expression above, $\mathrm{d}\ell_y = \{1 + (\partial_1 \bar{y}_2)^2\}^{1/2}\,\mathrm{d}\bar{y}_1$ is the differential arclength, $M_\alpha^\beta(\bar{\boldsymbol{r}})$ the transformed Green's function and $\bar{\partial}_\gamma \bar{\bar{\tau}}_{\beta\gamma}^{(l)}(\bar{\boldsymbol{y}})$ the divergence of the extra stress tensor in cylindrical co-ordinates, which is defined as:

$$\bar{\partial}_\gamma \bar{\bar{\tau}}_{\beta\gamma}^{(l)}(\bar{\boldsymbol{y}}) = g^{\alpha\beta}\left(\partial_\alpha \bar{\bar{\tau}}_{\beta\gamma}^{(l)} - \left\{ \begin{matrix} \lambda \\ \beta\alpha \end{matrix} \right\} \bar{\bar{\tau}}_{\lambda\gamma}^{(l)} - \left\{ \begin{matrix} \lambda \\ \gamma\alpha \end{matrix} \right\} \bar{\bar{\tau}}_{\beta\gamma}^{(l)} \right),$$

where the coefficients $\left\{ \begin{matrix} \lambda \\ \beta\alpha \end{matrix} \right\}$ are the Christoffel symbols of the first kind and $g^{\alpha\beta}$ is the contravariant metric tensor of the transformation [29]. In expression (2.16), the three-dimensional problem is reduced to a two-dimensional one. The presence of the non-Newtonian stress, however, makes it impossible to reduce the problem to one dimension as is possible for a purely Newtonian drop [11]. This implies that the computational effort required to solve non-Newtonian problems is considerably higher than for corresponding Newtonian problems. However, since only the volume of the drop needs to be discretized an efficient method can be arrived at compared with a conventional finite difference method.

With Equation (2.16), the authors have expressed the solution for the velocity field in the entire flow domain in terms of boundary and domain integrals, provided that the non-Newtonian stress tensor and the shape of the interface are given. The next section describes the complete method for solving the full time-dependent problem and show how the integral equation (2.16) is incorporated in this method.

3. NUMERICAL METHOD

In this section, the numerical method used to evaluate the boundary and domain integrals, the non-Newtonian stress tensor and the evolution of all surfaces $S^{(l)}$, $l = 1, \ldots, K$ are given in detail. In Section 3.1, the complete simulation method for the evolution of a drop consisting of K concentric layers of (non-)Newtonian material is described. The description of the geometry is provided in Section 3.2. The numerical method to calculate the velocity field, i.e. the evaluation of (2.16) is provided in Section 3.3. In Section 3.4, the time integration of the evolution equations (2.6) and (2.12) is presented.

3.1. Numerical algorithm

In anticipation of the numerical evaluation of the boundary integral formulation, a set of discrete collocation points is introduced in the internal domains $V^{(l)}$ and on the interfaces $S^{(l)}$. Using these discrete points, boundary elements are introduced to describe the shape of the interfaces and internal grid cells to cover the internal domains $\bar{V}^{(l)}$. In order to describe the state of the drop, both the non-Newtonian stress and the velocity need to be specified at these collocation points. At the start of the simulation, the stress is given by its initial conditions, whereas the velocity corresponding to the initial stress can be calculated using the boundary integral formulation for the velocity.

The complete procedure used to simulate the evolution of the non-Newtonian axisymmetric drop can be sketched as follows. Using the velocity given at time t and the evolution equation (2.12), one can calculate the new positions of the collocation points, and consequently the shape of the interfaces of the drop at $t + \Delta t$. Moreover, depending on the non-Newtonian model chosen, you either integrate (2.6) in time or calculate (2.7) explicitly in order to obtain the non-Newtonian stress tensor at the new time level. With this new stress tensor and shape of the interfaces, a new velocity field at time level $t+\Delta t$ can be calculated from (2.16). At this point, all the elements that describe the state of the drop, i.e. the collocation points describing the shape of the drop and the velocity and the non-Newtonian stress at these points, have advanced one time step. Repeating this explicit time integration procedure gives the evolution of the stress tensor, the velocity field and the shape of all the boundaries $\bar{S}^{(l)}$.

After imposing the initial condition for the non-Newtonian stress and the interfaces and after calculating the velocity field corresponding to this initial geometry and stress, the full algorithm can be summarized as follows:

1. update positions of the collocation points by integrating (2.12) over one time step to yield $\bar{S}^{(l)}(t+\Delta t)$, $l=1,\ldots,K$,
2. calculate the stress tensor at $t+\Delta t$ by solving (2.6) given $\bar{u}_\alpha$ at time t or by evaluating (2.7) using the new positions at time $t+\Delta t$,
3. calculate the velocity field at $t+\Delta t$ using (2.16) given $\bar{\bar{\tau}}_{\beta\gamma}$ and $\bar{S}^{(l)}$ from steps 1 and 2.

In the next three subsections, the representation of $S^{(l)}$ and $V^{(l)}$, the calculation of the velocity field and the time integration of both the non-Newtonian stress tensor and the boundaries will be discussed respectively.

3.2. Geometry description

The numerical implementation of the integrals in (2.16) requires an accurate representation of the interfaces $\bar{S}^{(l)}$ into $N_b^{(l)}$ boundary elements and the subdivision of the internal domains $\bar{V}^{(l)}$ into $N_c^{(l)}$ internal cells. For reasons of convenience, the superscript (l) is dropped whenever possible in this section.

Since the curvature of the interface is required in order to calculate the surface force $\bar{\boldsymbol{q}}$, higher-order boundary elements are used to represent the interfaces, whereas for the internal cells adopt quadrilateral elements are adopted. In order to be able to use standard integration techniques for the calculation of the domain integral, these quadrilateral elements are mapped to a standard square element using a bilinear transformation (Farin [30]):

$$\bar{\boldsymbol{X}}(s_1,s_2)=\bar{\boldsymbol{A}}_1(1-s_1)(1-s_2)+\bar{\boldsymbol{A}}_2 s_1(1-s_2)+\bar{\boldsymbol{A}}_3 s_1 s_2+\bar{\boldsymbol{A}}_4(1-s_1)s_2, \tag{3.1}$$

where $\bar{\boldsymbol{A}}_1$, $\bar{\boldsymbol{A}}_2$, $\bar{\boldsymbol{A}}_3$ and $\bar{\boldsymbol{A}}_4$ are the vertices of the quadrilateral element and s_1 and s_2 are the local co-ordinates of the corresponding standard element. For the higher-order boundary elements, piecewise C^2 cubic B-spline elements are used (DeBoor [31] and Farin [30]). The use of cubic B-spline elements requires a suitable parametrization of the curve along the collocation points, which is obtained with a chord length parametrization:

$$v[0]=0,$$

$$v[i]=v[i-1]+\|\bar{\boldsymbol{x}}_i-\bar{\boldsymbol{x}}_{i-1}\|,\quad i=1,\ldots,N_b,$$

where $\bar{\boldsymbol{x}}_i$ is the ith collocation point on the interface S. On this set of nodes a cubic B-spline curve $\bar{\boldsymbol{s}}$ is introduced as (DeBoor [31]):

$$\bar{\boldsymbol{s}}(v)=\sum_{j=-3}^{N_b-1}\bar{\boldsymbol{d}}_j B_j(v), \tag{3.2}$$

where $B_j(v)$ is a cubic B-spline and $\{\bar{\boldsymbol{d}}_j\}$ is the control vertices of the B-spline curve such that $\bar{\boldsymbol{s}}(v[i])=\bar{\boldsymbol{x}}_i$. It is noted that this interpolation problem can be fully specified if the symmetry of the drop is taken into account. The interpolation problem for $\bar{\boldsymbol{s}}(v)$ leads to a sparse matrix problem for $\{\bar{\boldsymbol{d}}_j\}$, which is solved using a band matrix solver.

From the control vertices $\{\bar{\boldsymbol{d}}_j\}$, first- and second-order derivatives, as well as points on the interface S, can be calculated using the DeBoor scheme [31]. The advantage of the DeBoor scheme is that you only use combinations of these control vertices, and do not have to evaluate the B-spline functions explicitly. From the first derivatives of the B-spline curve $\bar{s}$, the components of the normal vector are calculated using:

$$\bar{n}_1(v) = -\frac{1}{J}\partial_v \bar{s}_2, \qquad \bar{n}_2(v) = \frac{1}{J}\partial_v \bar{s}_1,$$

where J is the differential arclength of the curve:

$$J(v) = \sqrt{(\partial_v \bar{s}_1)^2 + (\partial_v \bar{s}_2)^2}\,. \tag{3.3}$$

The curvature $\bar{\partial}_\alpha \bar{n}_\alpha$ of the interface $\bar{S}$ of the drop is equal to the sum of the values of the curvatures in two arbitrary but mutually perpendicular directions. In case of an axisymmetric body described by cylindrical co-ordinates, it is most convenient to consider the curvatures in the meridian and azimuthal directions:

$$\bar{\partial}_\alpha \bar{n}_\alpha(v) = \frac{1}{(J)^2}\{\partial_{vv}\bar{s}_1\bar{n}_1 - \partial_{vv}\bar{s}_2\bar{n}_2\} + \left|\frac{n_2}{\bar{s}_2}\right|,$$

where a signed curvature [30] has been used for the meridian direction.

3.3. Calculation of the velocity

In order to calculate the velocity field, the integral equation (2.16) has to be solved at all the collocation points. If viscosity ratios in the layers differ from 1, a part of the Newtonian stress is incorporated into the non-Newtonian stress by redefining the non-Newtonian stress tensor as described in Section 2. However, by this procedure, the extra stress tensor becomes an explicit function of the velocity, which implies that (2.16) is solved iteratively at each time step. In this iteration, a trial velocity field that is used to calculate the Newtonian part of the extra stress tensor is assumed. Application of (2.16) yields a new velocity field, which serves as the trial velocity field for the next iteration step. This iteration procedure is applied, until the residual $R^{(n)}$ obtained after n iterations is smaller then a prespecified small number. The residual is defined as the discrete L_2 norm of the difference in the velocity at all collocation points in two successive iterations:

$$R^{(n)} = \left\|\bar{\boldsymbol{u}}^{(n)} - \bar{\boldsymbol{u}}^{(n-1)}\right\| \equiv \left\{\frac{1}{N_p}\sum_{i=1}^{N_p} |\bar{\boldsymbol{u}}_i^{(n)} - \bar{\boldsymbol{u}}_i^{(n-1)}|^2\right\}^{1/2}, \tag{3.4}$$

where $\bar{\boldsymbol{u}}^{(n)}$ is the velocity in the nth iteration level and N_p is the total number of collocation points. Computations showed that the iteration process can be stopped if the residual is smaller than 10^{-6}; more iterations do not effect the results. To reduce the required number of iterations, the initial trial velocity is set equal to the converged velocity obtained in the previous time step. In case all viscosities ratios $\lambda^{(l)}$ are equal to 1, the calculation reduces to a single step of this iteration procedure.

The velocity is computed at the collocation points, taken as the knots of the B-spline curve for the interfaces and as the vertices of the internal cells, using the integral expression (2.16). With the discretization of the boundaries and internal domains described above, one can rewrite (2.16) as:

$$\bar{u}_\alpha(\bar{\boldsymbol{x}}) \approx \bar{u}_\alpha^\infty(\bar{\boldsymbol{x}}) + \sum_{l=1}^{K}\sum_{m=1}^{N_C^{(l)}} \mathscr{I}_1(\bar{\boldsymbol{x}}; \bar{V}_m^{(l)}) + \sum_{l=1}^{K}\sum_{m=1}^{N_B^{(l)}} \mathscr{I}_2(\bar{\boldsymbol{x}}; S_m^{(l)}), \tag{3.5}$$

where $\mathscr{I}_1(\bar{x}; \bar{V}_m^{(l)})$ and $\mathscr{I}_2(\bar{x}; \bar{S}_m^{(l)})$ are integrals over the mth internal cell and the mth boundary element corresponding to the lth layer and interface respectively. Observe that $\mathscr{I}_1(\bar{x}; \bar{V}_m^{(l)}) = 0$ in case the lth layer consists of a Newtonian fluid and $\lambda^{(l)} = 1$. As the method to calculate the domain and interface integrals differ, both contributions are discussed separately, starting with the interface integral.

Using the spline curve $\bar{s}^{(l)}$ representation of the interface $\bar{S}^{(l)}$ one can rewrite $\mathscr{I}_2(\bar{x}; \bar{S}_m^{(l)})$ as:

$$\mathscr{I}_2(\bar{x}; \bar{S}_m^{(l)}) = \int_{\bar{S}_m^{(l)}} M_\alpha^\beta(\bar{r}) \bar{n}_\beta^{(l)}(\bar{y}) \bar{y}_2 \, \mathrm{d}\ell_y = \int_{v^{(l)}[m]}^{v^{(l)}[m+1]} M_\alpha^\beta(\bar{r}) \bar{n}_\beta^{(l)}(v) \bar{s}_2^{(l)}(v) J^{(l)}(v) \, \mathrm{d}v.$$

Green's function $M_\alpha^\beta(\bar{r})$ contains a logarithmic singularity as r tends to zero. This implies that $\mathscr{I}_2(\bar{x}; \bar{S}_m^{(l)})$ involves a singular integrand if $\bar{x}$ is located within the integration interval $\bar{S}_m^{(l)}$. A standard procedure used in the literature is to distinguish between regular and singular contributions (Toose *et al.* [26]). For the regular part, a standard quadrature rule is used, whereas the singular contributions are treated in a special manner. In this paper, the singularity in the integrand is removed in a uniform way that does not require a distinction between regular and singular contributions. To that end a quadratic transformation is used (Telles [32]):

$$v(\omega) = a\omega^2 + b\omega + c. \tag{3.6}$$

The constants a, b and c in (3.6) are determined such that the following conditions are met:

$$v(-1) = v^{(l)}[m], \qquad v(1) = v^{(l)}[m+1], \qquad \left. \frac{\partial v}{\partial \omega} \right|_{\tilde{v}^{(l)}} = 0. \tag{3.7}$$

where $\tilde{v}^{(l)}$ is defined as:

$$\tilde{v}^{(l)} = \{ v^{(l)} \in v^{(l)} \mid \| \bar{x} - \bar{s}^{(l)}(\tilde{v}^{(l)}) \| = \text{minimal} \}.$$

Transformation of (3.6) leads to:

$$\mathscr{I}_2(\bar{x}; \bar{S}_m^{(l)}) = \int_{-1}^{1} M_\alpha^\beta(\bar{r}) \bar{n}_\beta^{(l)}(v(\omega)) \bar{s}_2^{(l)}(v(\omega)) J^{(l)}(v(\omega)) \partial_\omega v \, \mathrm{d}\omega. \tag{3.8}$$

It is noted that the Jacobian $\partial_\omega v$ removes the singularity or quasi-singularity if $\bar{x}$ is located either in or outside the integration interval. The removal of the quasi-singularity leads to a higher accuracy, which is especially useful for drops with very thin layers. The resulting transformed integral in (3.8) is evaluated numerically using Gauss quadrature (Patridge [33] and Evans [34]).

In the remaining part of this section, the numerical evaluation of the domain integral is discussed. The domain integral $\mathscr{I}_1(\bar{x}; \bar{V}_m^{(l)})$ can be written as:

$$\begin{aligned} \mathscr{I}_2(\bar{x}; \bar{V}_m^{(l)}) &= \int_{\bar{V}_m^{(l)}} M_\alpha^\beta(\bar{r}) \bar{\partial}_\gamma \bar{\bar{\tau}}_{\beta\gamma}^{(l)}(\bar{y}) \bar{y}_2 \, \mathrm{d}\bar{y}_2 \, \mathrm{d}\bar{y}_1 \\ &= \int_0^1 \int_0^1 M_\alpha^\beta(\bar{r}) \bar{\partial}_\gamma \bar{\bar{\tau}}_{\beta\gamma}^{(l)}(\bar{X}(s_1, s_2)) \bar{X}_2(s_1, s_2) J_B^{(l)}(s_1, s_2) \, \mathrm{d}s_2 \, \mathrm{d}s_1, \end{aligned}$$

where the bilinear representation (3.1) of the mth quadrilateral element has been used and the Jacobian $J_B^{(l)}$ is given by:

$$J_B^{(l)} = \det\left(\frac{\partial \tilde{X}_\alpha(s_1, s_2)}{\partial s_\beta} \right).$$

Unlike the interface integrals, the authors now distinguish between two cases; (a) the internal cell does not contain the point $\bar{\boldsymbol{x}}$ and (b) the internal cell does contain the point $\bar{\boldsymbol{x}}$. In case (a), the domain integrand is regular and a normal Gauss quadrature is used to evaluate the integral. In case (b), the integrand is singular and a special treatment of the singularities in the kernels is required. To remove the singularity, the same quadratic transformation is used as was used for the boundary integral for both integration variables s_1 and s_2. After the removal of the singularity, a normal Gauss quadrature is used in both integration directions to evaluate the integral numerically.

With these numerical techniques, the authors have devised a second-order-accurate method to calculate the velocity of the stationary problem (2.16) in all collocation points. In the next section, the coupling of this solution with the time-dependent problem is discussed.

3.4. Time integration

In this section, the method to find the non-Newtonian stress tensor and the shape of the interface $\bar{S}^{(l)}$ at the new time level are discussed.

Updating the shape of the interface and the grid covering the lth layer $\bar{V}^{(l)}$ requires the calculation of the position of all the collocation points at the new time level. This calculation can be performed by time integration of (2.12) with an Euler forward scheme:

$$\bar{\boldsymbol{x}}_i(t_{n+1}) = \bar{\boldsymbol{x}}_i(t_n) + \Delta t \bar{\boldsymbol{u}}_i, \tag{3.9}$$

with $t_n = n\Delta t$, where Δt is a constant time step and $\bar{\boldsymbol{u}}_i$ is the velocity at the ith collocation point $\bar{\boldsymbol{x}}_i$. Moving the grid points in this way, however, may lead to a clustering of both internal and boundary grid points in certain regions and hence a highly deformed grid develops, leading to inaccurate results. The clustering arises directly from the fact that there are no restrictions on the stress tensor in tangential direction implying that the points can move freely along the interface in the direction of the external velocity field. To prevent the clustering of the collocation points, the boundary points are redistributed at every time step. To this end an auxiliary set of collocation points $\bar{\boldsymbol{y}}_i$ is introduced at the interface by:

$$\bar{\boldsymbol{y}}_i(t_{n+1}) = \bar{\boldsymbol{y}}_i(t_n) + \Delta t(\bar{\boldsymbol{u}}_i + \alpha_i^{(l)} \bar{\boldsymbol{t}}_i^{(l)}), \quad \bar{\boldsymbol{y}}_i \in \bar{s}^{(l)}, \tag{3.10}$$

where $\bar{\boldsymbol{t}}^i$ is the unit tangent vector along the lth interface (no summation over the index i). The coefficients $\alpha_i^{(l)}$ are determined such that:

$$\|\bar{\boldsymbol{y}}_{i+1} - \bar{\boldsymbol{y}}_i\|(\bar{\partial}_\gamma \bar{n}^j_\gamma(\bar{\boldsymbol{y}}_i) + \bar{\partial}_\gamma \bar{n}^j_\gamma(\bar{\boldsymbol{y}}_{i+1})),$$

is constant for all i at the new time level. By using this grid movement scheme, the points are redistributed in such a way that areas with high curvature have a somewhat higher concentration of grid points then areas with low curvature. The interior collocation points are found subsequently by generating a new grid at each time step. This is done by interpolation between the new auxiliary interface points on the interfaces $\bar{S}^{(l)}$ and $\bar{S}^{(l+1)}$. For a layer consisting of a viscoelastic model, however, one simply uses the Euler scheme (3.9), since the non-fading elasticity of the stress tensor compensates the viscous stress in the tangential direction, which prevents clustering of the collocation points.

The new non-Newtonian stress tensor in the numerical algorithm is obtained either by explicitly evaluating the stress (2.7) at the new time level or by integration of the constitutive equation (2.6), depending on the chosen model. In order to calculate the stress for the viscoelastic model, you need to evaluate the Cauchy–Green tensor (2.8), which requires the derivatives of the deformed grid with respect to a reference grid. For the reference grid, the grid at the initial time level, where the partial derivatives are evaluated using a second-order-accurate finite difference scheme, is used. Details concerning finite difference methods for curvilinear co-ordinates can be found in Thompson [35]. In case the non-Newtonian stress tensor is prescribed by a differential constitutive equation, the stress is integrated in time. To perform this integration for the Maxwell model, one has to evaluate the upper convected time derivative using a partial or a material time derivative. The use of the partial time derivative, however, leads to a convective term that is somewhat difficult to calculate. For this problem it is more convenient to use the material time derivative that does not require an explicit calculation of the convective term. This implies that the new non-Newtonian stress tensor $\bar{\bar{\tau}}_{\beta\gamma}$ will be defined on the grid that is convected according to (3.9). Integration of (2.6) with an Euler forward scheme leads to:

$$\bar{\bar{\tau}}_{\beta\gamma}(t_{n+1}) = \bar{\bar{\tau}}_{\beta\gamma}(t_n) + \Delta t(g^{\nu\mu}[\bar{\partial}_\nu \bar{u}_\beta(t_n)\bar{\bar{\tau}}_{\mu\gamma}(t_n) + \bar{\bar{\tau}}_{\beta\nu}(t_n)\bar{\partial}_\mu \bar{u}_\gamma(t_n)] + \bar{R}_{\beta\gamma}(t_n)), \tag{3.11}$$

with $g^{\nu\mu}$ the metric tensor and $\bar{R}_{\beta\gamma}$ given by:

$$\bar{R}_{\beta\gamma}(t_n) = \frac{\lambda^{(p)}}{\mu}\left(\bar{\partial}_\beta \bar{u}_\gamma(t_n) + \bar{\partial}_\gamma \bar{u}_\beta(t_n)\right) - \frac{1}{\mu}\,\bar{\tau}^{NN}_{\beta\gamma}(t_n). \tag{3.12}$$

The covariant derivative $\bar{\partial}_\beta$ in (3.11) and (3.12) is defined as [29]:

$$\bar{\partial}_\beta \bar{u}_\gamma = \frac{\partial \bar{u}_\gamma}{\partial \bar{x}^\beta} - \left\{ \begin{matrix} \xi \\ \gamma\beta \end{matrix} \right\} \bar{u}_\xi, \tag{3.13}$$

As an alternative to the first-order Euler scheme, a second- or higher-order Runge–Kutta scheme can be used.

Due to the Lagrangian approach the new stress tensor $\bar{\bar{\tau}}_{\beta\gamma}(t_{n+1})$ resulting from (3.11) is defined on the grid whose positions are given by (3.9). In order to find it on the new grid $\bar{\boldsymbol{y}}_i$ the stress tensor is interpolated by:

$$\bar{\bar{\tau}}_{\beta\gamma}(\bar{\boldsymbol{y}}_i) \approx \frac{1}{\sum_{j\in J} 1/(D_{ij})^2} \sum_{j\in J} \frac{\bar{\bar{\tau}}_{\beta\gamma}(\bar{\boldsymbol{x}}_j)}{(D_{ij})^2}, \tag{3.14}$$

with $D_{ij} = |\bar{\boldsymbol{y}}_i - \bar{\boldsymbol{x}}_j|$ and the summation $j\in J$ involves all the indices of the nearest neighbours of the grid point $\bar{\boldsymbol{y}}_i$. To ensure that this interpolation is sufficiently accurate, a time step restriction is introduced:

$$\Delta t = \varepsilon \min_n \left\{ \frac{\Delta \bar{x}_n}{\bar{u}_n} \right\}, \tag{3.15}$$

where $\Delta \bar{x}_n$ is the shortest side of the nth internal cell, $\bar{u}_n$ the mean velocity over this element and ϵ is of the order 0.1.

4. RESULTS AND DISCUSSION

This section presents the results of numerical calculations to validate and illustrate the method. For the validation of the numerical method a grid refinement study is performed and the numerical results are compared with available analytical results known from the literature.

Although the method can be used for drops with many layers, here focus is on drops with either one or two layers (i.e. $K = 1$ or 2 respectively). The one layer drop is discussed in Section 4.1, whereas the results for the two layer drop are presented in Section 4.2. In order to remove

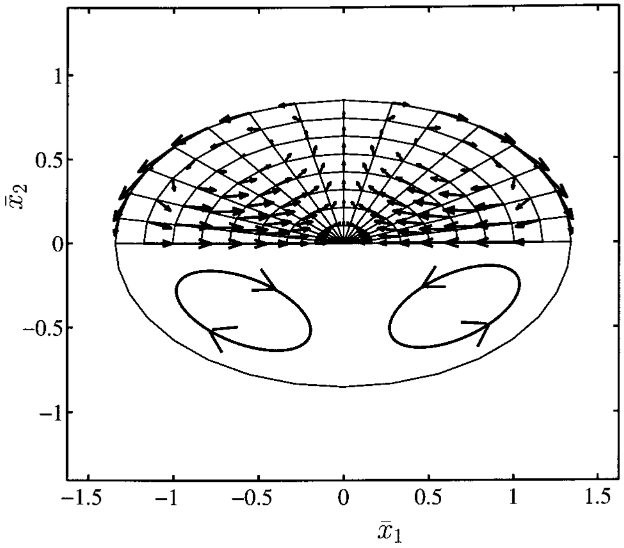

Figure 2. The velocity profile and grid of a single layer viscous drop with $\lambda^{(1)}=1$ at $C^{(1)}=0.1$. In the lower part of the figure the vortices that are present in the velocity profile are drawn schematically.

the effects of the deformation history of the drop, the relaxed state of the non-Newtonian stress tensor at $t=0$ (i.e. $Q=0$ in Equation (2.13)) is used.

4.1. Singe layer non-Newtonian drop

In this section, the authors study the response of an axisymmetric drop containing an Oldroyd-B fluid or a viscoelastic material to an elongational flow. Before turning to the validation of the method, a typical example of a deformed drop and the corresponding velocity field is shown.

In Figure 2, a vector plot of the steady state velocity field of a fluid-like drop (i.e. viscous or Oldroyd-B drop) at $C=0.1$ is drawn. In the velocity field, one can distinguish two vortices, which are also drawn schematically in the lower part of the figure. For the viscoelastic drops, no vortices exist since the velocity becomes zero in the steady state due to the non-fading elasticity of the viscoelastic material.

Investigation of the order of accuracy of the numerical method is performed using grid refinement (Toose [25]). Suppose you have numerically obtained the solution at a certain time to on a given grid. The deformation $D(t_0)$ should asymptotically converge to its analytical value at a specific rate in case the grid is refined. The order of accuracy of the method can be obtained from the values of $D(t_0)$ on subsequent refinement levels of the grid. Especially the values of the convergence rate ρ_i, defined by:

$$\rho_i=\frac{D_{(i+1)}-D_{(i)}}{D_{(i+2)}-D_{(i+1)}}, \quad \text{for} \quad i\geq 0, \tag{4.1}$$

on the set of grids is of importance in this respect. Here $D_{(i)}$ is the deformation of the drop on the ith refinement level at time t_0. The grid is usually refined with a Romberg sequence, in which the grid spacing is halved at each refinement. It is, however, more efficient to use a Bulirsch sequence consisting of two intertwined Romberg sequences (Stoer [36]). Table 1 presents typical grid refinement results for an Oldroyd-B drop with $\lambda_p=5$ and $\mu_p=1$ using the deformation at $t_0 = 1$ at two different values of the capillary number. Analyzing the convergence behaviour of the deformation, it is found that the method is second-order-accurate in space for this specific case. Besides a rapid convergence, the method also gives very good results for relatively coarse grids. Using a similar refinement study for the time step, it is found that accuracy in time is first-order for the Euler and second-order for the compact storage four stage Runge–Kutta scheme (Jameson [37]). To provide a way to verify the correctness of the numerical method, the authors compare their numerical results with theoretical results from the literature and investigate several limiting cases of the non-Newtonian stress tensor.

The Oldroyd-B model contains three independent parameters, the viscosity ratios λ and λ_p and the dimensionless relaxation time μ_p. If either λ_p or μ_p approaches zero, an essentially Newtonian behaviour results [26]. Numerical calculations showed that the limiting behaviour of the Oldroyd-B drop is correctly recovered. To verify the results for moderate values of λ_p and μ_p, theoretical results obtained by Delaby *et al.* [38] are used. The theoretical background for these results is based on the linear theory for viscous emulsions of Oldroyd [12], which has recently been extended to viscoelastic emulsions by Palierne [14]. This linear theory starts with the solution to the Stokes equation in terms of an expansion in spherical harmonics [8]. By approximating the shape interface in terms of spherical harmonics one can use the boundary conditions of the problem to find the leading order shape correction. The amplitude of this correction for the radial displacement of the interface, is given by:

$$A(\omega) = \frac{5G_\mathrm{d}^*(19G_\mathrm{d}^* + 16G_\mathrm{o}^*)}{(2G_\mathrm{d}^* + 3G_\mathrm{o}^*)(19G_\mathrm{d}^* + 16G_\mathrm{o}^*) + C(G_\mathrm{d}^* + G_\mathrm{o}^*)}, \tag{4.2}$$

where G_d^* and G_o^* are the complex moduli of the drop fluid and outer fluid respectively. In case of an Oldroyd-B drop placed in a viscous fluid, the complex moduli G_d^* and G_o^* are given by:

$$G_\mathrm{d}^* = \mathrm{i}\omega\lambda + \frac{\mathrm{i}\omega\lambda_p}{1 + \mathrm{i}\omega\mu_p}, \qquad G_\mathrm{o}^* = \mathrm{i}\omega,$$

with i the imaginary unit and ω the frequency of the oscillations of the external flow. The amplitude $A(\omega)$ can also be written in the form:

$$A(\omega) = A_\infty\left(1 - \sum_j \frac{B_j}{1 + \mathrm{i}\omega\mu_j}\right),$$

where the coefficients B_j, relaxation times μ_j of the deformation process and A_∞ are evaluated numerically for particular values of the parameters. The response of the deformation to an elongational velocity is then given by:

Table 1. Grid refinement results of the deformation of an Oldroyd-B drop ($\lambda_p^{(1)} = 5$ and $\mu_p^{(1)} = 1$) at $t_0 = 1$ for two different capillary numbers ($C^{(1)} = 0.01$ and 0.1)

Grid		Deformation ($t = 1$)	
N_b	N_c	$C = 0.01$	$C = 0.1$
16	80	0.016311	0.15152
24	168	0.016504	0.15262
32	288	0.016569	0.15299
48	624	0.016611	0.15323
64	1088	0.016625	0.15330

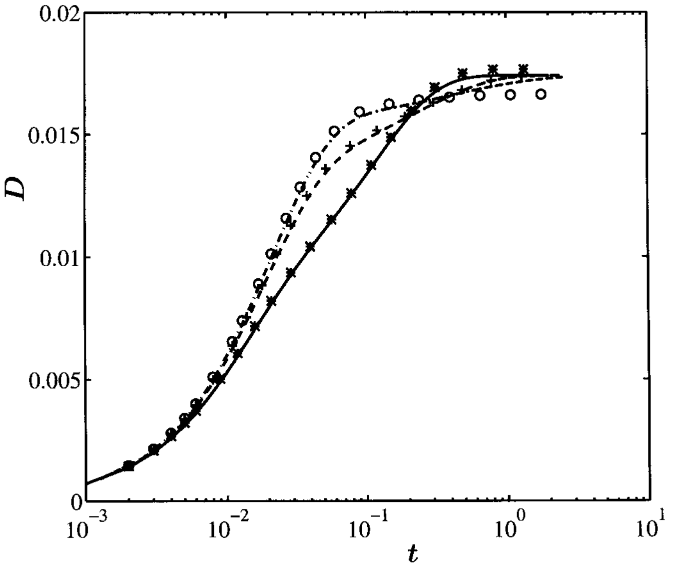

Figure 3. The deformation of an Oldroyd-B drop at $C^{(1)} = 0.025$ for three values of the relaxation time $\mu_p^{(1)}$. The viscosity ratio $\lambda_p^{(1)}$ is kept constant at 5. The dash–dotted, dashed and solid lines represent the analytical results for $\mu_p^{(1)} = 1$, 0.25 and 0.0625 respectively. The circles, pluses and asterisks display the corresponding numerical results.

$$D(t) = \frac{3A_\infty C}{4}\left\{\left(1 - \sum_j B_j\right)t + \sum_j B_j\mu_j(1 - \mathrm{e}^{-t/\mu_j})\right\}. \tag{4.3}$$

Figure 3 shows a plot of expression (4.3) for three values of the relaxation time μ_p and $\lambda_p = 5$ of the Oldoyd-B fluid and some corresponding numerical results. The numerical results were generated using a grid with 48 boundary elements and 624 cells in the internal domain. For small values of the relaxation time of the Oldroyd-B model, the analytical and numerical results are in good agreement. The steady state deformation of the analytical solution for small relaxation times of the Oldroyd-B model lies somewhat below the numerically obtained values. Comparison with a second-order theory for viscous drops (Barthès-Biesel [10]) reveals that the numerically obtained steady state deformation is correct and that the linear theory slightly underpredicts this deformation. For higher values of μ_p, there are some discrepancies between the analytical and numerical results that cannot be explained by shortcomings in the first-order theory. In this case, the differences are caused by the non-linear character of the upperconvected time derivative in the constitutive equation for the Maxwell model. In order to establish this, a simulation performed with a linear time derivative is considered and it is observed that the numerical and analytical results were in better agreement. Analyzing this equation, it was observed that the non-linearity increases with increasing relaxation time of the model, which explains why the discrepancies increase with increasing relaxation time. The overall agreement, however, is very satisfactory.

The viscoelastic model, given in (2.7), contains two independent parameters, c_1 and c_2. In this section, two cases are considered: the viscoelastic I and the viscoelastic II models. To verify the results, the authors use theoretical results obtained by Roscoe [15] for viscoelastic spheres. Assuming that the shape of the drop remains ellipsoidal in time, the longest axis $r_{\max}$ of the drop follows from the following non-linear equations [15]:

$$\begin{cases} \dfrac{5}{4} g_2(r_{\max}^2 - r_{\max}^{-1}) = \dfrac{5}{2c_1} & \text{for} \quad c_2 = 0, \\ \dfrac{5}{4} g_2(r_{\max} - r_{\max}^{-2}) = \dfrac{5}{2c_2} & \text{for} \quad c_1 = 0, \end{cases} \tag{4.4}$$

where g_2 is defined by (Jeffery [16]):

$$g_2 = \int_0^\infty \frac{z \, \mathrm{d}z}{(r_{\max}^2 + z)(r_{\max}^{-1} + z)\{(r_{\max}^2 + z)(r_{\max}^{-1} + z)^2\}^{1/2}}.$$

By evaluating g_2 numerically for several values of $r_{\max}$, the relationship between the deformation D and the constants c_1 or c_2 can be found, since D can be calculated from $r_{\max}$, and by the assumption that the shape remains ellipsoidal and the incompressibility of the fluid. In Figure 4, the numerical and analytical results for the steady state deformation of a drop consisting of a viscoelastic I or II material have been plotted. For the numerical calculations, a grid with 16 boundary elements and 128 cells in the internal domain has been used. For all values of c_1 and c_2, the analytical and the numerical results are in very good agreement. Both models have the same behaviour for small deformations (i.e. large values of c_1 or c_2) and differ strongly for large deformations. Especially, the viscoelastic II drop shows strong non-linear behaviour for larger deformation, which is well-captured by the numerical method.

From this it can be concluded that the method gives correct results for a drop consisting of an Oldroyd-B fluid or a viscoelastic material. It is also found that the method is capable of dealing with large deformations and strong non-linear behaviour of the non-Newtonian stress tensor. The next section concentrates on a drop composed of two layers.

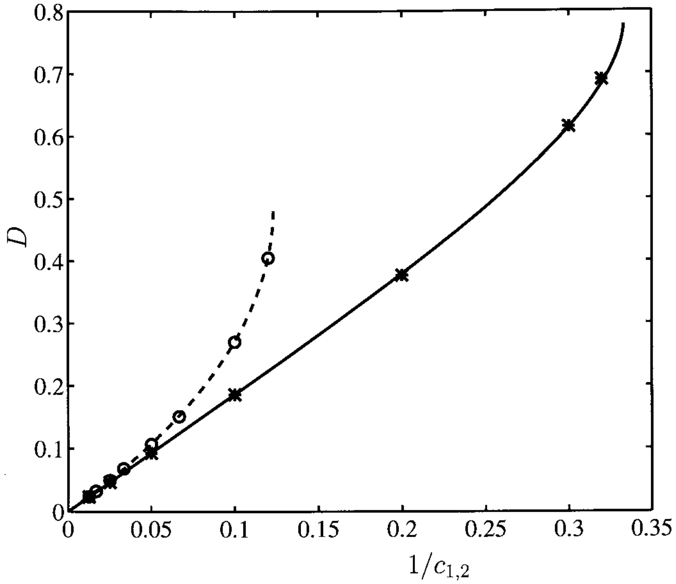

Figure 4. Steady state deformation of a viscoelastic drop with $\lambda^{(1)} = 1$ for a constant value of either $c_1^{(1)}$ or $c_2^{(1)}$. The solid and dashed lines represent the analytical results for $c_2^{(1)} = 0$ and $c_1^{(1)} = 0$ respectively. The asterisks and circles display the corresponding numerical results.

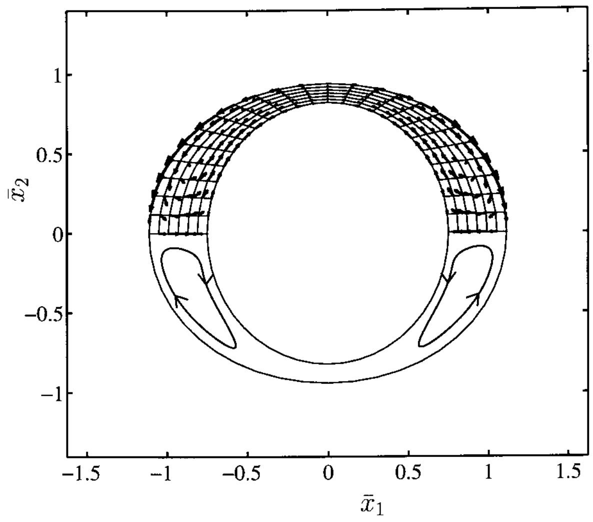

Figure 5. The velocity profile and grid of a double layer viscous drop with $\lambda^{(1)} = \lambda^{(2)} = 1$. The initial thickness of the outer interface is 0.2 and the capillary number at both interfaces is equal to 0.1. In the lower part of the figure, the vortices that are present in the outer viscous layer are drawn schematically.

4.2. Double layer non-Newtonian drop

This section presents some simulation results for a drop consisting of two layers of material. The internal layer $V^{(2)}$ consists of a viscous fluid with $\lambda^{(2)} = 1$ and the outer layer $V^{(1)}$ of the drop contains a (non-)Newtonian material. At the present moment only analytical results for a drop where $V^{(2)}$ consists of a viscous or a viscoelastic material are known to the authors. For this reason, they restrict themselves to these two situations and do not discuss a drop where $V^{(2)}$ contains an Oldroyd-B fluid, although the method is perfectly suitable for this situation as well.

As for the single layer drop, attention is first turned to a typical example of a double layer drop. In Figure 5, the steady state velocity field and grid of a viscous drop with $C^{(1)} = C^{(2)} = 0.025$ and $\lambda^{(1)} = 1$ is plotted. In the second layer, two vortices are present that are also drawn schematically in the lower part of the figure. It is seen that these vortices deform the inner interface in a direction opposite to the deformation of the outer interface. Due to this mechanism, the layer $V^{(1)}$ is thicker at the tops of the drop and thinner in the middle part of the drop. Stone and Leal [11] suggest that a contact of the interfaces leads to break-up of the drop. The steady state deformation of a drop where $V^{(1)}$ consists of a viscoelastic I material with $c_1^{(1)} = 80$ differs substantially from a viscous drop as can been seen in Figure 6. In this figure, no velocity field is plotted as it is zero in the steady state situation. Due to the elastic nature of the material there is almost no variation of the thickness of the layer $V^{(1)}$, and hence break-up is not caused by contact of the two interfaces. At this moment, a break-up mechanism based on critical stresses in the viscoelastic layer is developed. Results concerning this mechanism will be published in the near future.

Using grid refinement it is found that the order of accuracy for the double layer drop is the same as for the single layer drop, i.e. second-order in space and first- or second-order in time, depending on the time integration method used. To verify the results for a drop consisting of two viscous layers, small deformation results obtained by Stone and Leal [11] are used. The theory leading to these results is based on the work of Taylor [7] for single layer drops and

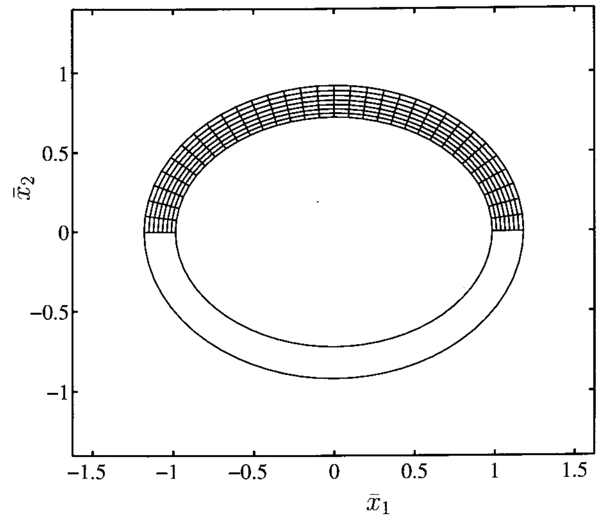

Figure 6. The grid of a two layer drop with a viscous ($\lambda^{(1)} = 1$) inner and a viscoelastic outer layer ($\lambda^{(1)} = 1$, $c_1^{(1)} = 80$ and $c_2^{(1)} = 0$). The initial thickness of the outer interface is 0.2.

shows strong resemblance with the theories discussed in the previous section. In this case, expressions are obtained for the amplitude of the radial displacement of both interfaces from which the deformation can be derived. In Figure 7 the analytical and numerical steady state deformation of both interfaces are plotted as a function of the initial shell thickness $\kappa^{(1)}$ at $C = 0.025$. The numerical results were generated with 32 boundary elements along both

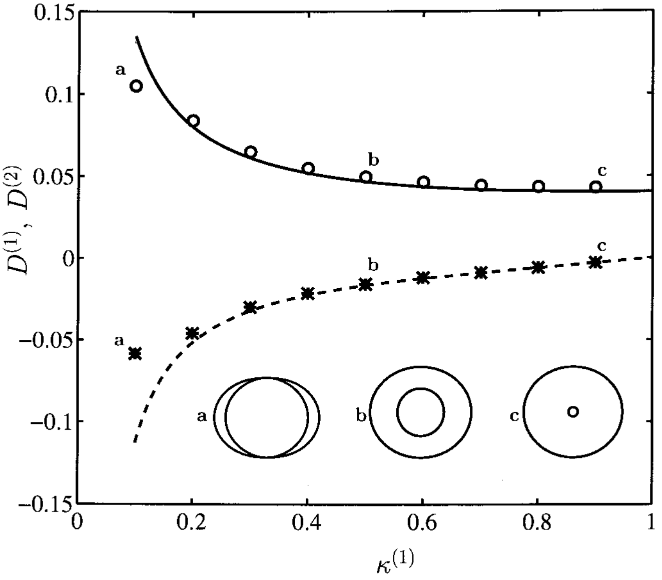

Figure 7. Steady state deformation of a two layer viscous drop with $\lambda^{(1)} = \lambda^{(2)} = 1$ at $C^{(1)} = 0.025$ vs. the initial interface thickness $\kappa^{(1)}$. The circles and crosses represent the numerically obtained deformations of the inner and outer interface respectively. The solid and dashed lines display the corresponding analytical results. The steady state configurations for $\kappa^{(1)} = 0.1$, 0.5 and 0.9 are also contained in the plot.

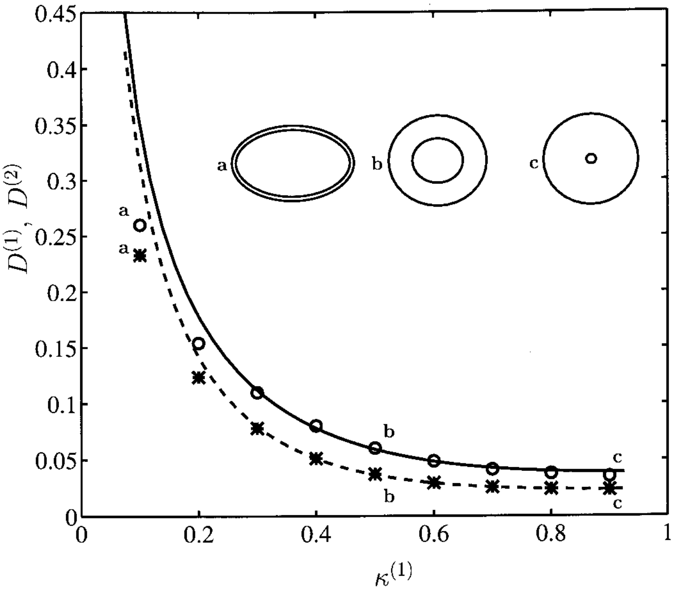

Figure 8. Steady state deformation of a two layer drop with a viscous interior $\lambda^{(2)} = 1$ and a viscoelastic ($\lambda^{(1)} = 1$, $c_1^{(1)} = 80$ and $c_2^{(1)} = 0$) outer layer at $C^{(1)} = 0.025$ vs. the initial interface thickness $\kappa^{(1)}$. The circles and crosses represent the numerically obtained deformations of the inner and outer interface respectively. The solid and dashed lines display the corresponding analytical results. The steady state configurations for $\kappa^{(1)} = 0.1$, 0.5 and 0.9 are also contained in the plot.

interfaces and no internal cells since there is no domain integral present in this particular case. Also plotted in the figure are the steady state shapes of the drop for three different values of the thickness $\kappa^{(1)}$. The numerical and analytical results are in excellent agreement for small deformations with relative deviation below 1% in case $\kappa^{(1)} > 0.5$. For larger deformations, i.e. smaller $\kappa^{(1)}$, there are some differences that can be explained by the limited validity of the linear theory. The relative deviation of the numerical results compared with the linear theory rapidly increases to about 25% as $\kappa^{(1)}$ becomes smaller than about 0.2, and the results show an overprediction of the deformation by the linear theory. The authors further investigated this discrepancy and considered the case in which the ratio between the viscous stress and the surface tension was decreased. This has the effect of reducing the deformation of the compound Newtonian drop. At smaller deformations, the correspondence between the simulation data and the linear theory indeed improves, which adds to the validation of the present method. The shapes in this figure clearly show that break-up can already occur for very small deformations of the outer interface, as was also remarked by Stone and Leal [11].

The results for a drop consisting of a viscous inner layer and a viscoelastic I outer layer are verified using analytical first-order results by Brunn [5]. In this theory, the Navier–Stokes and Navier equations are used to describe the displacement fields of the viscous and elastic layer respectively. The derivation of the amplitude of the radial displacement of both interfaces is analogous to the theories described above. Figure 8 plots the analytical and numerical results for the steady state deformation as a function of the initial thickness of the viscoelastic I layer with $c_1^{(1)} = 80$. In order to keep the aspect ratio of the internal cells limited, different grids for different values of $\kappa^{(1)}$ (e.g $N_b^{(1)} = N_b^{(2)} = 32$, $N_c^{(1)} = 160$ for $\kappa^{(1)} = 0.1$ and $N_b^{(1)} = N_b^{(2)} = 16$, $N_c^{(1)} = 256$ for $\kappa^{(1)} = 0.9$) have been used. Figure 8 also plots the shapes of the drop for several values of $\kappa^{(1)}$. From these plots it is observed that the interfaces deform uniformly for all $\kappa^{(1)}$.

It is seen, similar to a completely viscous double layer drop, that the numerical and analytical results are in good agreement for small deformations. Additional computations that were performed for higher values of $c_1^{(1)}$ (i.e. smaller deformations) lead to smaller differences at $\kappa^{(1)} = 0.1$, indicating independently that the discrepancies are due to the limited validity of the linear theory. This is further illustrated in Figure 9, which compares numerical results for the steady state deformation of a two layer with linear theory.

From this it can be concluded that the method developed in Sections 2 and 3 gives correct results for a double layered (non-)Newtonian drop. Also found are very interesting results concerning the thickness of the outer layer pointing towards essentially different break-up mechanisms for different composing materials. This will be studied in more detail in the near future.

5. CONCLUSIONS

In this paper a boundary integral method for axisymmetric multilayered non-Newtonian drops immersed in a viscous fluid subjected to an axisymmetric flow was presented. The non-Newtonian contribution was treated as a source term, leading to a domain integral in the boundary integral representation of the solution. By transforming the integral representation for the velocity to cylindrical co-ordinates the authors can reduce the dimension of the computational problem. The integral equation for the velocity remains of the same form and Green's functions are transformed explicitly to cylindrical co-ordinates. Simulations show that the numerical method developed is second-order-accurate in space and first- or second-order-accurate in time depending on the time integration scheme used.

The numerical results for a single and double layered (non-)Newtonian drop have been compared with analytical results known from the literature. The time-dependent behaviour of a single layer Oldroyd-B drop is in good agreement with analytical results for small values of

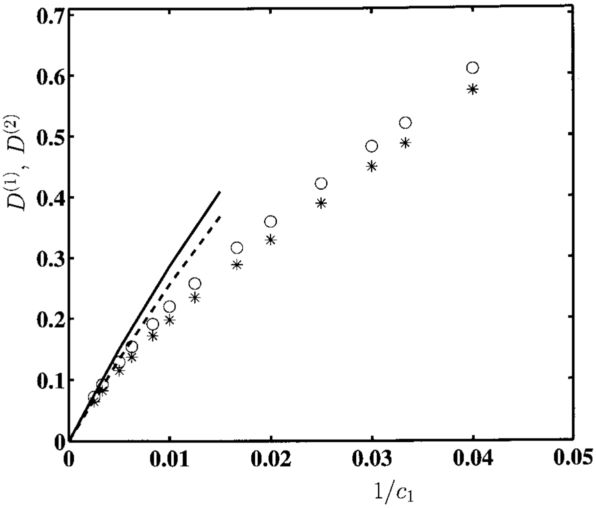

Figure 9. Steady state deformation of a two layer drop with a viscous interior $\lambda^{(2)} = 1$ and a viscoelastic I outer layer ($\lambda^{(1)} = 1$, $\kappa^{(1)} = 0.1$) vs. the ratio between the viscous and elastic forces. The circles and asterisks represent the numerically obtained deformations of the inner and outer interface, respectively. The solid and dashed lines display the corresponding analytical results.

the relaxation time (Delaby *et al.* [38]). For a drop containing an elastic material, the steady state behaviour was examined. It was found that the numerical and analytical results are in excellent agreement with each other and that strong non-linear behaviour of the drop is well-captured by the method. The numerical results for the steady state behaviour of a double layer drop consisting of a viscous inner layer and a viscous or viscoelastic outer layer is in good agreement with analytical results. The thickness of a viscous outer layer varies strongly along the interface, whereas the thickness of a viscoelastic layer remains almost uniform. This implies that the break-up mechanism due to contact of the interfaces is unlikely to be relevant for viscoelastic layers. In this case the introduction of a critical break-up stress in the viscoelastic layer seems a more plausible mechanism. This will be studied in the future.

The boundary integral method developed in this paper is well-suited for compound non-Newtonian drops although computational times are much longer than in the Newtonian case due to the domain integral that appears in the formulation. The advantage of the method over a more direct (finite difference) discretization of the Stokes equations lies in the fact that only the non-Newtonian layers of the drop have to be discretized and that calculations using relatively few points already give very accurate results. In case of thin layers the advantages of the method can be fully exploited since only small part of the total flow domain has to be discretized. Conversely, the present method is not expected to be very efficient in case large regions of the flow domain contain non-Newtonian material or if non-linear terms can not be neglected and the Navier–Stokes equations should be used. In such cases a finite difference or finite element method may be computationally cheaper. Moreover, if the deformation of non-Newtonian drops becomes extreme then special attention should be paid to retaining the grid sufficiently smooth and properly clustered. During extreme deformations the grid may become too skewed or stretched, which has a negative influence on the accuracy. An incorporation of dual reciprocity [33], which removes the need to evaluate the domain integrals with a cell-by-cell integration, may partly resolve these complications and may add to the efficiency of the method.

ACKNOWLEDGMENTS

This work was supported by the J.M. Burgers Centre under EZ-project P-22. The authors wish to thank Dr R.M.J. van Damme for his help on the B-spline formulation and the grid movement scheme and Dr H.T.M. van den Ende, Professor J. Mellema and Professor P.J. Zandbergen for several stimulating discussions.

REFERENCES

1. J.M. Rallison, 'The deformation of small viscous drops and bubbles in shear flow', *Annu. Rev. Fluid Mech.*, **16**, 45–66 (1984).
2. H.A. Stone, 'Dynamics of drop deformation and break-up in viscous fluids', *Annu. Rev. Fluid Mech.*, **26**, 65–102 (1994).
3. H.A. Lorentz, 'Eene algemeene sterling omtrent de beweging eener vloeistof met wrijving en eenige daaruit afgeleide gevolgen', *Versl. K Akad. W. Amsterdam*, **5**, 168–175 (1896).
4. O.A. Ladyzhenskaya, *The Mathematical Theory of Viscous Incompressible Flow*, Gordon and Breach, New York, 1969.
5. P.O. Brunn, 'The deformation of a viscous particle surrounded by an elastic shell in a general time-dependent linear flow field', *J. Fluid Mech.*, **126**, 533–544 (1983).
6. J.B.A.F. Smeulders, The mechanical properties of lipid bilayers, *Ph.D. Thesis*, University of Twente at Enschede, 1992.
7. G.I. Taylor, 'The viscosity of a fluid containing small drops of another fluid', *Proc. R. Soc. A.*, **146**, 41–48 (1932).
8. H. Lamb, *Hydrodynamics*, Dover, New York, 1932.

9. R.G. Cox, 'The deformation of a drop in a general time-dependent fluid flow', *J. Fluid Mech.*, **37**, 601–623 (1969).
10. D. Barthès-Biesel, 'Deformation and burst of a liquid droplet freely suspended in a linear shear field', *J. Fluid Mech.*, **61**, 1–21 (1973).
11. H.A. Stone and L.G. Leal, 'Break-up on concentric double emulsion droplets in linear flows', *J. Fluid Mech.*, **211**, 123–156 (1990).
12. J.G. Oldroyd, 'The elastic and viscous properties of emulsions and suspensions', *Proc. Roy. Soc. A*, **218**, 122–132 (1953).
13. J.G. Oldroyd, 'The effects of interfacial stabilizing films on the elastic and viscous properties of emulsions', *Proc. Roy. Soc. A*, **232**, 567–577 (1955).
14. J.F. Palierne, 'Linear rheology of viscoelastic emulsions with interfacial tension', *Rheol. Acta*, **29**, 204–214 (1990); Erratum **30**, 497 (1991).
15. R. Roscoe, 'On the rheology of a suspension of viscoelastic spheres in a viscous liquid', *J. Fluid Mech.*, **28**, 273–293 (1967).
16. G.B. Jeffery, 'The motion of ellipsoidal particles immersed in a viscous fluid', *Proc. Roy. Soc. A*, **102**, 161–179 (1922).
17. G.K. Youngren and A. Acrivos, 'Stokes flow past a particle of arbitrary shape: a numerical method of solution', *J. Fluid Mech.*, **69**, 377–403 (1975).
18. Q. Huang and T.A. Cruse, 'Some notes on singular integral techniques in boundary element analysis', *Int. J. Numer. Methods. Eng.*, **36**, 2643–2659 (1993).
19. M. Tjahjadi, H.A. Stone and J.M. Ottino, 'Satellite and subsatellite formation in capillary break-up', *J. Fluid Mech.*, **243**, 297–317 (1992).
20. H.A. Stone and L.G. Leal, 'The effects of surfactants on drop deformation and break-up', *J. Fluid Mech.*, **220**, 161–186 (1990).
21. Xiofan Li, R. Charles and C. Pozrikidis, 'Simple shear flow of suspensions of liquid drops', *J. Fluid Mech.*, **320**, 395–416 (1996).
22. M. Loewenberg and E.J. Hinch, 'Numerical simulation of a concentrated emulsion in shear flow', *J. Fluid Mech.*, **321**, 395–419 (1996).
23. M.B. Bush, J.F. Milthorpe and R.I. Tanner, 'Finite element and boundary element methods for extrusion computations', *J. Non-Newt. Fluid Mech.*, **16**, 37–51 (1984).
24. M.B. Bush, R.I. Tanner and P. Phan-Thien, 'A boundary element investigation of extrude swell', *J. Non-Newt. Fluid Mech.*, **18**, 143–162 (1985).
25. E.M. Toose, R.M.J. van Damme, H.T.M. van den Ende, B.J. Geurts and J.M.G. Kuerten, 'A boundary element method for two-dimensional (non-)Newtonian drops in slow viscous flow', *J. Non-Newt. Fluid Mech.*, **60**, 129–154 (1995).
26. E.M. Toose, D. van den Ende, B.J. Geurts, J.G.M. Kuerten and P.J. Zandbergen, 'Axisymmetric non-Newtonian drops treated with a boundary integral method', *J. Eng. Math.*, **30**, 131–150 (1996).
27. X.Z. Li, D. Barthès-Biesel and A. Helmy, 'Large deformations and burst of a capsule freely suspended in a elongational flow', *J. Fluid Mech.*, **187**, 179–196 (1988).
28. C. Pozrikidis, *Boundary Integral and Singularity Methods for Linearized Viscous Flow*, Cambridge University Press, New York, 1992.
29. R.B. Bird, R.C. Amstrong and O. Hassager, *Dynamics of Polymeric Liquids: Volume 1 Liquid Mechanics*, Wiley-Interscience, New York, 1987.
30. G. Farin, *Curves and Surfaces for Computer Aided Geometric Design; A Practical Guide*, Academic Press, San Diego, 1990.
31. C. DeBoor, *A Practical Guide to Splines*, Springer, New York, 1978, p. 392.
32. J.C.F. Telles, 'A self-adaptive co-ordinate transformation for efficient numerical evaluation of general boundary element integrals', *Int. J. Numer. Methods Eng.*, **24**, 959–973 (1987).
33. P.W. Patridge, C.A. Brebbia and L.C. Wrobel, *The Dual Reciprocity Boundary Element Method*, Computational Mechanics Publications, Boston, 1992.
34. G. Evans, *Practical Numerical Integration*, Wiley, Guildford, 1993.
35. J.F. Thompson, Z.U.A. Warsi and W.C. Mastin, *Numerical Grid Generation: Foundations and Applications*, North-Holland, New York, 1985.
36. J. Stoer, *Einführung in die numerische Mathematik I*, Springer, Berlin, 1976.
37. A. Jameson, 'Transonic flow calculations', *MAE-Report 1651*, Princeton University, 1983.
38. I. Delaby, B. Ernst and R. Muller, 'Drop deformation during elongational flow in blends of viscoelastic fluids; small deformation theory and comparison with experimental results', *Rheol. Acta*, **34**, 525–533 (1995).